ACS EARTH AND SPACE CHEMISTRY
http://pubs.acs.org/journal/aesccq
Article

Intercalation of Water in Kaolinite ($Al_2Si_2O_5(OH)_4$) at Subduction Zone Conditions: Insights from Raman Spectroscopy

Abhisek Basu* and Mainak Mookherjee

Cite This: *ACS Earth Space Chem.* 2021, 5, 834−848

Read Online

ACCESS | Metrics & More | Article Recommendations | SI Supporting Information

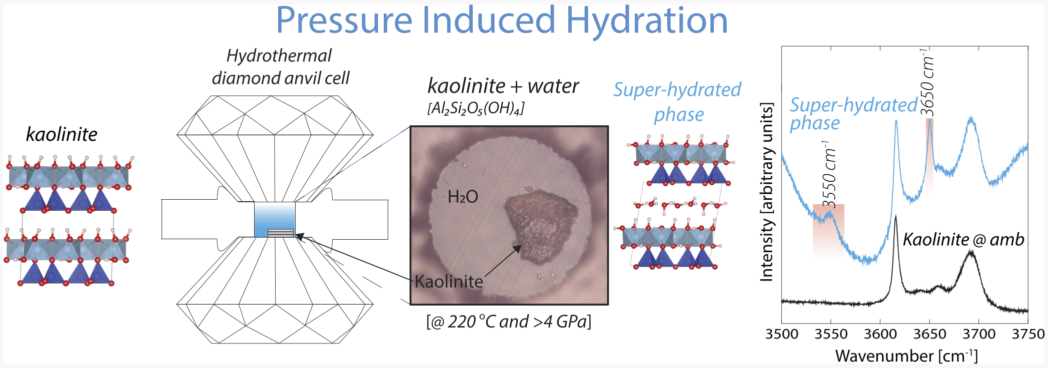

ABSTRACT: Kaolinite ($Al_2Si_2O_5(OH)_4$) is produced by weathering of continental rocks and is an important constituent of terrigenous sediment flux in subduction zone. It helps in transporting water into the Earth's interior. Kaolinite consists of a layer of silicate tetrahedral (Tet) sheet and a layer of octahedral (Oct) sheet. There are two distinct crystallographic environments for protons: an inner hydroxyl group and an inner surface hydroxyl group that holds together adjacent Tet-Oct layers by hydrogen bonds. We investigate the high-pressure behavior of these two distinct proton environments upon compression up to 9 GPa using a diamond anvil cell and Raman spectroscopy. Upon compression, the hydroxyl stretching region exhibits major changes as kaolinite transitions from the low pressure phase K-I to the intermediate pressure phase K-II at ∼2.9 GPa, and the intermediate pressure phase K-II to the high-pressure phase K-III at ∼6.1 GPa. These are associated with significant changes in the pressure dependence of the hydroxyl modes, thus reflecting the changes in the hydrogen bonding environment (O-H···O) between the adjacent Tet-Oct···Tet layers. The K-I phase exhibits strengthening of hydrogen bonds between the Tet-Oct···Tet layers, i.e., $\frac{d\nu_{OH}}{dP} < 0$. The K-II phase exhibits significantly reduced hydrogen bond strength between the Tet-Oct···Tet layers, i.e., $\frac{d\nu_{OH}}{dP} > 0$. Based on the static DAC results, we hypothesize that, owing to the reduced strength of hydrogen bonding in the interlayer region of the K-II phase, it acts as a precursor for the super-hydrated kaolinite, where water molecules are intercalated in the interlayers of the K-II phase. To test this hypothesis, we conducted high pressure (P)-temperature (T) experiments with kaolinite and water at conditions relevant to the subduction zones. We explored up to a maximum pressure of ∼4.5 GPa and temperatures up to ∼350 °C. Irrespective of the P-T path undertaken, i.e., compression followed by heating or heating followed by compression, upon cooling "kaolinite + water", we found the appearance of new vibrational modes at ∼3550 and 3650 cm^{-1}. These new vibrational modes are related to the intercalated water molecules in the super-hydrated kaolinite. This super-hydrated kaolinite phase is likely to subduct significantly more water than the K-I phase.

KEYWORDS: *high pressure, kaolinite, super-hydrated kaolinite, hydrogen bond, Raman spectroscopy, diamond anvil cell (DAC), hydrothermal diamond anvil cell (HDAC) subduction zone*

■ INTRODUCTION

Interaction of the hydrosphere with the continental crust is manifested in weathered rocks and minerals, composed primarily of layered hydrous silicates including clays. For instance, the average mineralogical composition of the continental crust near the surface can be assumed to be albite ($NaAlSi_3O_8$), which weathers to layered silicates such as kaolinite ($Al_2Si_2O_5(OH)_4$).[1,2] It is estimated that, on an annual

Received: December 20, 2020
Revised: February 12, 2021
Accepted: February 19, 2021
Published: March 12, 2021

https://dx.doi.org/10.1021/acsearthspacechem.0c00349

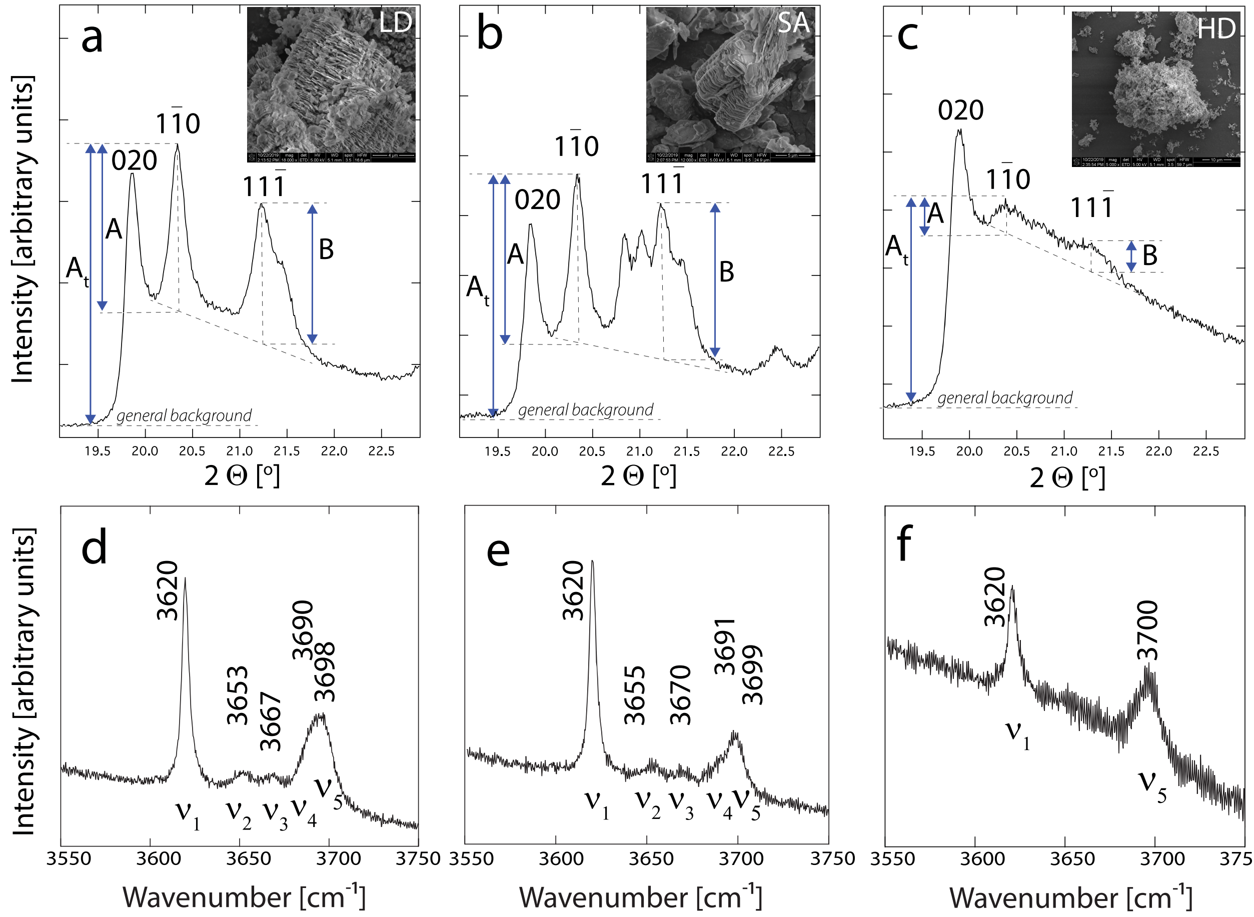

Figure 1. Plot shows the X-ray diffraction pattern for kaolinite clays for (a) low defect (LD) kaolinite from West Georgia, (b) commercially obtained sample from Sigma Aldrich (SA), and (c) high defect (HD) kaolinite from West Georgia. Based on XRD results, we determined the Hinckley index (H_i), where A and B refers to the intensity from $1\bar{1}0$ and $11\bar{1}$ reflection, respectively. The intensity is measured with respect to the inter-peak background. In contrast, A_t refers to the intensity of $1\bar{1}0$ reflection, measured from the general background. Inset shows the corresponding scanning electron microscopy images. A lower H_i for the HD sample, ~0.3, is explained by a rather poor crystallinity of the sample. Also shown are the Raman spectra of the hydroxyl stretching region between 3550 and 3750 cm^{-1}. (d) LD kaolinite from West Georgia, (e) SA kaolinite, and (f) HD kaolinite from West Georgia. The laser power used for all the Raman spectra for all the samples, i.e., LD, SA, and HD, shown in this figure was <5%. The ν_1 mode corresponds to "inner hydroxyl" and ν_i ($i = 2 - 5$) corresponds to the "inner surface" hydroxyl group.

basis, around 2×10^{13} kg of weathered crustal rocks from the continents are transported to the ocean basins.[3] Although it is predicted that the abundance of kaolinite (~7.8 wt % water) varies between 5 and 60% in oceanic sediments,[4,5] the sediment may also contain other layered hydrous silicates with water contents between 12 and 14%. This would mean that the sediments in the ocean basin are capable of subducting (1.5−2.6) $\times 10^{12}$ kg/yr of water. Estimates based on deep-sea drilling have also shown that the amount of sediment that is subducted is of the order of (1−2) $\times 10^{12}$ kg/yr.[6] In this estimated sediment mass, the terrigenous sediments constitute the major portion and the contribution from carbonate is rather minor.[7] Thus, it is estimated that ~1 $\times 10^{12}$ kg/yr of water locked in the layered hydrous silicates could be subducted.[7] It is very likely that a portion of the subducted water is lost back to the surface via island arc volcanism, and the remaining portion of the water is subducted further into the deep Earth. The net water contribution from the hydrated oceanic crust is estimated to be greater than the contributions from the layered hydrous minerals in the subducted sediments and altered continental crustal components.[8] The layered hydrous silicates stabilized in more mafic compositions have limited thermal stability.[9] In contrast, the hydrous phases stabilized in alumina and silica-rich lithology as in Al_2O_3-SiO_2-H_2O (ASH) ternary often have greater thermal stability and hence, although volumetrically minor, may provide an effective mechanism of transporting water into the deep Earth in warmer subduction zones.[10]

Thus, it is apparent that understanding the high-pressure behavior, in particular, the elastic and thermodynamic properties of layered hydrous silicates, is quite important for our understanding of how water is transported into the deep Earth. So far, significant research has been conducted to better understand the structure and the atomistic scale evolution of the structure of kaolinite and its polymorphs,[11−20] which in turn influences the thermoelastic properties.[17,20]

In a recent study, pressure-induced hydration has been observed in a natural sample of kaolinite and its polymorph using synchrotron X-rays and infrared spectroscopy at pressures and temperatures relevant for subduction zones.[21,22] While intercalation in layered hydrous silicates and clays have received considerable attention, this recent study is one of the first reports of such intercalation in kaolinite at high pressures and temperatures. A key question is, if the adjacent T:O layers of layered hydrous silicate are held by a weak hydrogen bond, then at high pressures, it is expected that the hydrogen bonds are strengthened since it is well known that compression in layered hydrous silicates are very anisotropic, i.e., the compression of the basal layer is significantly greater compared to other directions. If so, the pressure-induced hydration in the basal layer is rather counterintuitive.

To better understand this issue, we explore the high-pressure behavior of kaolinite with a special emphasis on how pressure might influence the behavior of protons, pressure dependence of hydrogen bonding, and how that might aid pressure-induced hydration. We also explore the intercalation of water in kaolinite at high pressure and temperature conditions along different P−T pathways.

■ METHOD

To examine the high-pressure−temperature behavior of kaolinite using Raman spectroscopy, we have examined three kaolinite samples: a "high-defect" (HD) and a "low-defect" (LD) kaolinite from Warren County, GA, and a sample obtained from Sigma Aldrich (SA). The Warren County kaolinite samples were obtained from Source Clays Repository, Clay Mineral Society. At ambient P−T, we characterized the HD, LD, and SA samples using a Rigaku Smart Lab X-ray diffractometer with a copper (Cu) source (λ = 1.54 Å), 40 kV of voltage, and 30 mA. We have collected Raman spectra using a Horiba Jobin Yvon LabRam HR Evolution spectrometer. The spectrometer uses a thermoelectrically cooled CCD detector with a ~2 cm^{-1} spectral resolution. In the Raman spectrometer setup, the samples were excited using a 532 nm laser from a frequency-doubled Nd-YAG lasing crystal with a maximum power output of 300 mW. We used a long working distance 50× objective lens and 1800 lines/mm grating. At ambient conditions, we explored the high-energy region dominated by hydroxyl (O−H) stretching between 3400 and 3800 cm^{-1} for SA, LD, and HD kaolinite samples. In comparison to the LD and SA kaolinite samples, which had five well-defined modes in the O−H stretching region, the HD kaolinite exhibited poorly defined modes, which are likely due to the low degree of order and poor crystallinity as reflected in X-ray diffraction (XRD) and back-scattered electron (BSE) images (Figure 1). The degree of disorder in clays are often characterized by the Hinckley index (H_i)[23,24] defined as: $H_i = \frac{A+B}{A_t}$, where A and B refers to the intensity from $1\bar{1}0$ and $11\bar{1}$ reflection, respectively. The intensity is measured with respect to the inter-peak background. In contrast, A_t refers to the intensity of the $1\bar{1}0$ reflection, measured from the general background (Figure 1). The Hinckley index, H_i often ranges between 1.44 and 0.18, with values lower than 0.43 representing kaolinite samples with a higher proportion of defects and a higher value of H_i representing well-ordered defect-free samples.[23] We find that the H_i for the LD and SA kaolinite samples to be 1.02 and 1.33, respectively. Both LD and SA represent well-ordered samples in agreement with previous studies.[23,24] In contrast, we find that H_i for the HD sample is ~0.23, indicating a rather poor crystallinity. We also supplemented XRD data by collecting back-scattered electron (BSE) images using a scanning electron microscope (SEM) (Figure 1). We used an FEI Nova 400 NanoSEM with an operational voltage of 5.0 kV and a working distance of ~5.0 mm. The BSE images indicate a good layer stacking and crystallinity of SA and LD kaolinite samples, corroborating with the higher H_i determined from the XRD measurements. In contrast, at a similar higher magnification, the HD kaolinite samples did not exhibit stacked layering (Figure 1).

To explore the effect of laser power, we collected the Raman spectra of the LD and SA samples at ambient conditions by increasing the laser power in incremental steps. We collected the Raman spectra at ambient conditions, in two distinct settings: (1) the powder sample pressed on a glass slide and (2) the sample confined inside a diamond anvil cell gasket chamber with the pressure cell just locked by its weight (Supporting Information, Figures SF1−SF4). Based on the effect of laser power on the sample, we selected 30 mW, i.e., 10% laser power, at the source for acquiring Raman spectra. We kept the laser power constant throughout the high-pressure measurements. To understand the effect of laser power on the Raman spectrum, we have also collected a temperature-dependent Raman spectrum of LD and SA samples from 350 K down to 90 K using a Linkam THMS 600 stage with a quartz window. The Linkam THMS 600 stage was cooled with a constant flow of liquid nitrogen (N_2). For the low-temperature measurements, we used a laser power of 0.1%. We also performed a test with varying laser power on the sample in the Linkam THMS 600 stage and noted that the quartz window did not absorb the laser (Supporting Information, Figures SF5and SF6).

Due to the poor crystalline quality of the HD kaolinite and low H_i (~0.23), we did not explore the HD sample any further. We explored the LD and SA kaolinite samples at high pressures for static compression. We used a symmetrical diamond anvil cell (DAC) for the high-pressure measurements. In the symmetric DAC, we used two low fluorescence diamonds with a culet size of 300 μm. We used a 150 μm thick stainless-steel gasket to contain the kaolinite sample. We pre-indented the stainless-steel gasket to 50 μm in thickness. We used an Almax−Boehler μ-driller to drill a sample cavity of 100 μm in diameter at the center of the pre-indented gasket. We collected Raman spectra up to ~9 GPa, i.e., well within the hydrostatic limit of a 4:1 methanol−ethanol mixture, which was used as pressure media.[25,26] We used the ruby fluorescence line for the pressure calibration[27] with an error of ±0.1 GPa. To understand the mechanism of intercalation of water, we loaded LD kaolinite in a hydrothermal diamond anvil cell (HDAC).[28,29] For the high pressure and temperature experiments using HDAC, we used a pair of low-fluorescence diamonds with a culet size of ~500 μm. The low fluorescence diamonds were hosted in a tungsten carbide (WC) seat. To resistively heat the sample chamber, we used a molybdenum (Mo) wire coiled around the tungsten carbide (WC) seats. We measured the temperature using two K-type thermocouples attached to the diamonds and close to the sample chamber. We programmed the power delivered to the upper and the lower heater molybdenum coils by using an integrated power controller from PES Enterprise. The variation in the temperature between the upper and lower diamond and the set temperature was <±1 °C during the heating and cooling cycles. The maximum temperature reached in the present set of experiments was 350 °C. We loaded the sample chamber with micron-sized ruby grains for pressure calibration during high-pressure and temperature experiments. We placed the ruby grains at a distance from the kaolinite inside the sample chamber so that the intense ruby fluorescence did not interfere with the Raman signal from the kaolinite and water. We flushed the cell with an argon (98%)− hydrogen (2%) gas mixture to prevent the diamond and the heater wire from oxidation. The absorbed moisture, if any, in kaolinite was removed by placing the sample overnight in an oven at ~100 °C. To load the sample in the hydrothermal diamond anvil cell (HDAC), we compressed the powdered kaolinite sample between two diamonds to create a

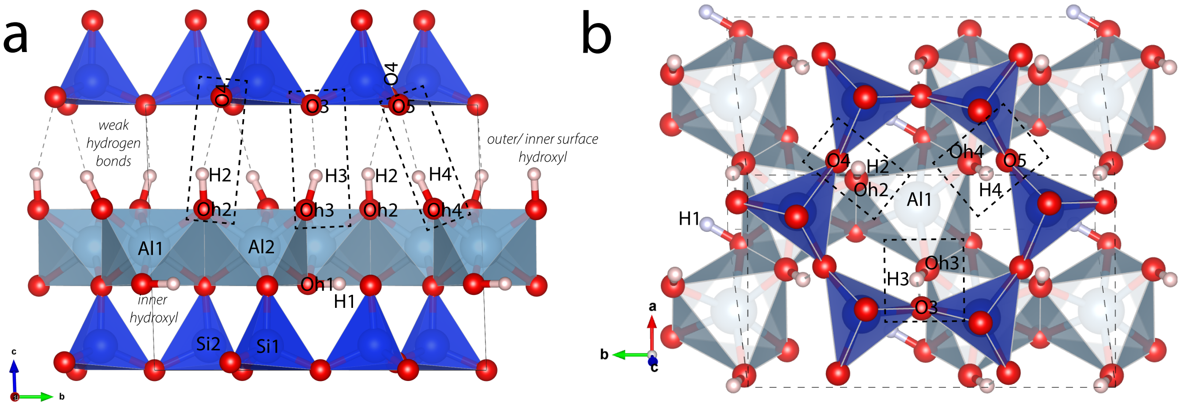

Figure 2. Crystal structure of kaolinite (a) projected down *a* axis, i.e., showing the *b*−*c* plane, and (b) projected down *c** axis showing the octahedral layer and the overlying tetrahedral layer joined by hydrogen-bonded pairs. The crystal structure of kaolinite consists of a tetrahedral layer attached with an octahedral layer (T-O) attached to the adjacent tetrahedral layer by weak hydrogen bonds (denoted by dashed gray lines). The position of the hydrogen atoms (denoted by light pink spheres, H1, H2, H3, and H4), silicon atoms (denoted by dark blue spheres, Si1 and Si2), aluminum atoms (denoted by light blue spheres, Al1 and Al2), and the oxygen atoms (denoted by red spheres) are from a crystal structure refinement study.[14]

thin flake (∼10−20 μm in thickness) and added a small drop of water using a micro-syringe. We used HPLC grade water in all the HDAC experiments. A slow stream of compressed air was used to cool the objective lens.

■ RESULTS

Hydroxyl Stretching Region at Ambient Conditions. To understand the Raman spectra of hydroxyl stretching region for kaolinite, it is useful to relate the spectra with the crystal structure of kaolinite. The crystal structure of kaolinite consists of a silicate tetrahedral (T) layer attached to an octahedral (O) layer (Figure 2). In the tetrahedral layers, silicate tetrahedral units are arranged to form six-membered di-trigonal rings[14,30,31] with a fundamental repeat unit of $[Si_2O_5]^{2-}$. The fundamental unit of the octahedral layer consists of two trivalent aluminum ions (Al^{3+}), i.e., di-octahedral layer, with a stoichiometry of gibbsite $Al(OH)_3$. The adjacent tetrahedral and octahedral layers are held together with weak hydrogen bonds. Neutron diffraction studies at low temperatures (∼1.5 K) have revealed four crystallographically distinct hydrogen positions.[14] One of the hydroxyl vectors [Oh1-H1] is oriented near parallel to the (001) layer, and the hydrogen atom (H1) is located in the di-octahedral cavity often referred to as the "inner hydroxyl" (Figure 2). The typical bond distance for [Oh1-H1] at ambient conditions is ∼0.974 Å.[14,19] The other three hydroxyl vectors, i.e., [Oh2-H2, Oh3-H3, and Oh4-H4] are near perpendicular to the (001) layer. Also, these three hydroxyl vectors form a weak hydrogen bond between the octahedral layer and the adjacent basal oxygen atoms of the tetrahedral layer. These three hydroxyl vectors are often referred to as the "inner surface" or "outer" hydroxyl group (Figure 2). The hydroxyl bond distance and angle involving the Oh2-H2····O4 hydrogen-bonded pairs at low-temperature conditions are Oh2-H2 ≈ 0.982 Å; H2····O4 ≈ 2.145 Å, Oh2····O4 ≈ 3.087 Å, and the angle Oh2-H2 makes with the (001) plane is ∼73.16°.[14,19] The hydroxyl bond distance and angle involving the Oh3-H3····O3 hydrogen-bonded pairs at ambient condition are Oh3-H3 ≈ 0.976 Å; H3····O3 ≈ 2.039 Å, Oh3····O3 ≈ 2.980 Å, and the angle Oh3-H3 makes with the (001) plane is ∼68.24°.[14,19] The hydroxyl bond distance and angle involving the Oh4-H(4)····O(5) hydrogen-bonded pairs at ambient condition are Oh4-H4 ≈ 0.975 Å; H4····O5 ≈ 2.041 Å, Oh4····O5 ≈ 2.945 Å, and the angle Oh4-H4 makes with the (001) plane is ∼60.28°.[14,19]

We note that, at ambient conditions, the Raman spectra for the hydroxyl stretching region for LD kaolinite reveal five distinct modes located at 3620 cm^{-1} (ν_1), 3653 (ν_2), 3667 (ν_3), 3690 (ν_4), and 3698 (ν_5) (Figure 1 and Table 1). The Raman spectra of SA kaolinite is also characterized by five distinct modes located at 3620 cm^{-1} (ν_1), 3655 (ν_2), 3670 (ν_3), 3691 (ν_4), and 3699 (ν_5) (Figure 1 and Table 1). In an idealized crystal structure of kaolinite, the four unique OH groups, i.e.,

Table 1. Deconvoluted Peak Positions, Widths, and Relative Intensities of the OH-Stretching Modes from the Collected Raman Spectra of Three Kaolinites: LD, SA, and Keokuk[a]

position [cm^{-1}]	FWHM [cm^{-1}]	relative intensity [%]
	LD	
3620	4.0	48.7
3653	7.3	3.6
3667	14.1	7.0
3690	13.8	7.2
3698	11.8	33.5
	SA	
3620	4.4	46.4
3655	19.3	13.7
3670	7.5	2.5
3691	17.0	14.6
3699	9.8	22.8
	HD	
3621	1.0	56
3696	1.0	44
	Dry KGa-1 kaolinite[15]	
3621	5.6	25.2
3652	14.3	10.1
3668	7.9	4.2
3688	13.6	27.0
3696	12.5	33.5
	Dry Mesa Alta kaolinite[15]	
3621	5.1	22.8
3652	11.3	10.4
3668	9.1	5.3
3686	13.5	34.9
3696	12.8	26.7

[a] The present data are compared to previously obtained values.[15]

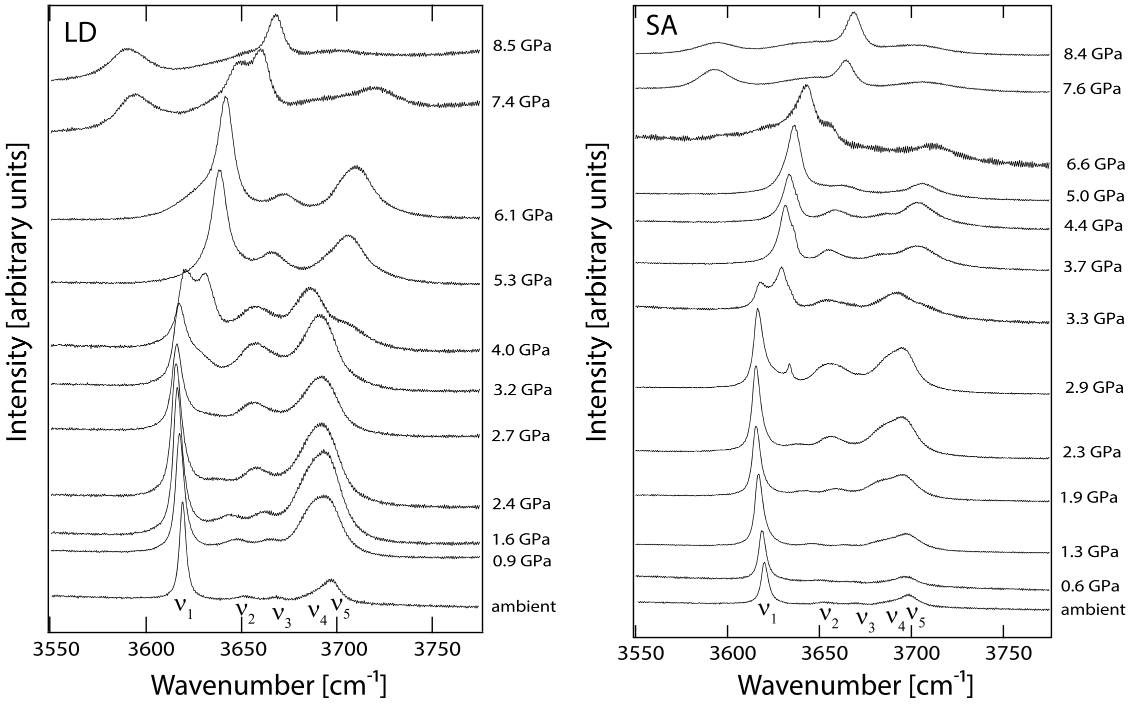

Figure 3. Plot shows a stack of pressure-dependent Raman spectra of the hydroxyl stretching region (~3550−3800 cm^{-1}) of LD kaolinite and SA kaolinite. For the evolution of modes upon compression, refer to Supporting Information, Figure SF7.

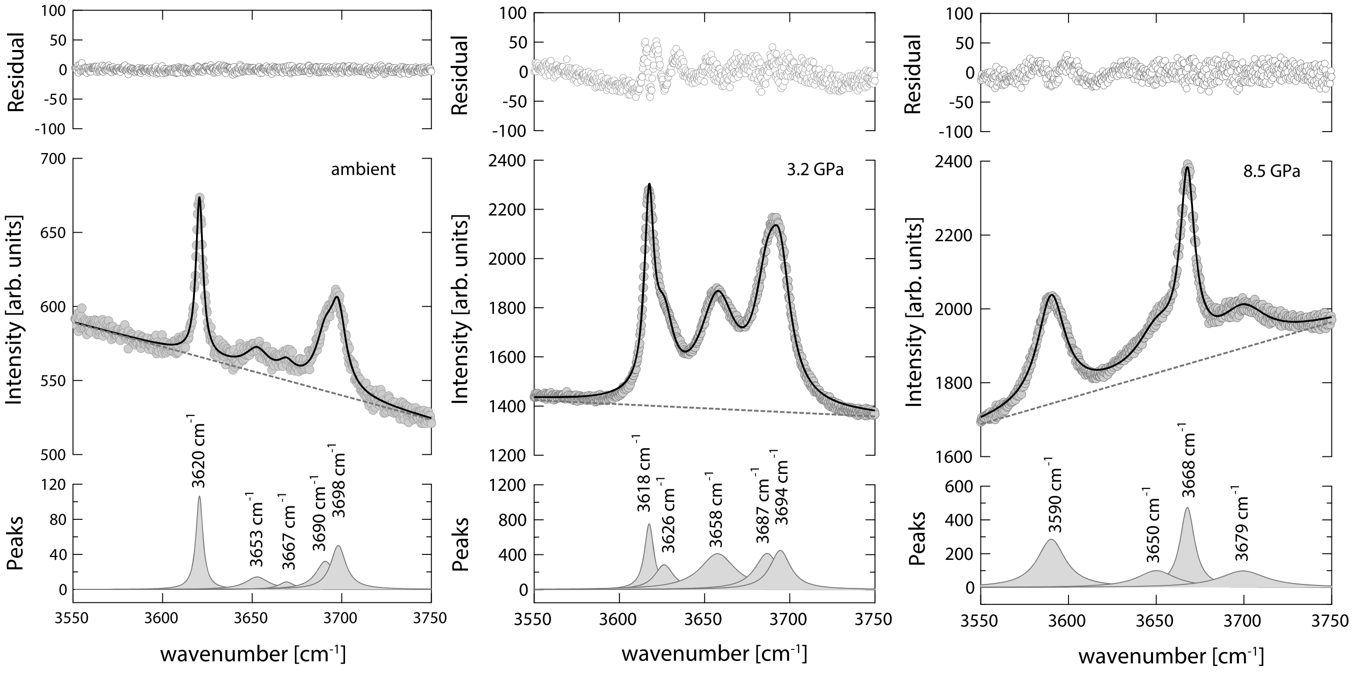

Figure 4. Raman spectra of the hydroxyl stretching region for LD kaolinite at ambient conditions show five distinct peaks at 3620 cm^{-1} (ν_1), 3653 cm^{-1} (ν_2), 3667 cm^{-1} (ν_3), 3690 cm^{-1} (ν_4), and 3698 cm^{-1} (ν_5); at 3.2 GPa, five distinct peaks at 3618 cm^{-1} (ν_1), 3626 cm^{-1} (ν_2), 3658 cm^{-1} (ν_3), 3687 cm^{-1} (ν_4), and 3694 cm^{-1} (ν_5); and at 8.5 GPa, four distinct peaks at 3590 cm^{-1} (ν_1), 3650 cm^{-1} (ν_2), 3668 cm^{-1} (ν_3), and 3679 cm^{-1} (ν_4). For the SA kaolinite sample at similar conditions, refer to Supporting Information, Figure SF8.

Oh1-H1, Oh2-H2, Oh3-H3, and Oh4-H4,[14,19] are likely to produce four distinct OH stretching frequencies. Infrared spectroscopic studies have shown four distinct O−H stretching modes that are related to these distinct hydroxyl environments.[18,32−34] The assignment of the OH modes with the independent hydroxyl group is consistent with theoretical predictions based on density functional theory.[35]

The lowest energy mode ν_1 corresponds to the vibration associated with the "inner hydroxyl" group, i.e., [Oh1-H1] (Figure 2). The higher energy O−H stretching modes (ν_2, ν_3, and ν_5) are related to the "inner surface" hydroxyls. These three higher energy O−H stretching modes have been often assigned to the coupled symmetric and asymmetric vibrational motions related to the "inner surface" hydroxyls.[11,32] However, these

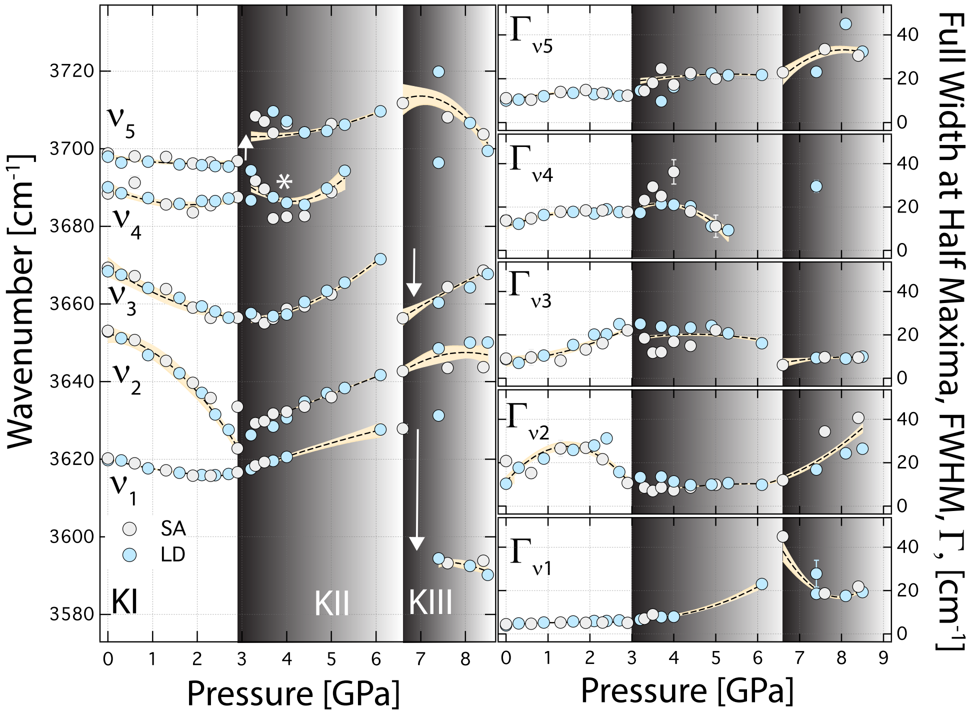

Figure 5. Plot of the pressure dependence of the peak positions and the full width at half maxima of the OH stretching modes of LD (filled light blue circles) and SA (open gray circles) kaolinite obtained by deconvolution of the spectra at all the pressures explored in this study. Three distinct phases of kaolinite are evident, low-pressure K-I followed by high-pressure phases identified as K-II and K-III at pressures of ~2.9 and 6.5 GPa, respectively. The K-I to K-II and K-II to K-III transitions are shown with gray shadings. The minima in the ν_4 and ν_5 mode frequency in the K-II phase is represented by an asterisk.

Table 2. Pressure Dependence of the Hydroxyl Vibrational Modes in Kaolinite and Coefficients of Polynomial Expansions[a]

i	$\nu_i(P)$	$\sigma\nu_i(P)$	$\nu_i'(P)$	$\sigma\nu_i'(P)$	$\nu_i''(P)$	$\sigma\nu_i''(P)$	$\Gamma_i(P)$	$\sigma\Gamma_i(P)$	$\Gamma_i'(P)$	$\sigma\Gamma_i'(P)$	$\Gamma_i''(P)$	$\sigma\Gamma_i''(P)$
K-I kaolinite												
1	3620.1	0.05	−3.16	0.11	0.58	0.04	4.18	0.05	1.27	0.11	−0.30	0.04
2	3652.3	2.22	−1.76	4.18	−2.86	1.33	11.17	2.22	22.35	4.18	−7.64	1.33
3	3669.5	2.54	−7.44	3.31	1.01	0.96	7.74	2.54	1.55	3.31	1.24	0.96
4	3690.2	1.48	−5.21	2.40	1.47	0.77	11.00	1.48	6.77	2.40	−1.54	0.77
5	3697.9	0.70	−1.74	1.15	0.43	0.39	9.92	0.70	4.14	1.15	−1.13	0.39
K-II kaolinite												
1	3616.9	0.60	4.02	1.30	−0.18	0.46	6.93	0.60	−0.32	1.30	1.75	0.46
2	3627.8	0.15	4.44	0.21	0.01	0.07	5.73	0.15	2.98	0.21	−0.48	0.07
3	3655.8	1.04	0.90	1.46	1.39	0.43	18.15	1.04	2.95	1.46	−1.01	0.43
4	3691.9	1.97	−9.75	3.97	4.35	1.75	18.93	1.97	7.72	3.97	−5.58	1.75
5	3703.2	1.53	−0.38	1.57	0.79	0.37	18.50	1.53	3.19	1.57	−0.70	0.37
K-III kaolinite												
1	3592.2	11.80	3.40	17.00	−1.98	5.70	41.55	5.29	−33.83	7.68	11.67	2.64
2	3642.0	1.46	7.38	5.77	−2.47	3.10	12.20	0.71	6.94	1.38	2.49	1.13
3	3656.0	2.45	7.17	3.64	−0.40	1.28	6.80	2.45	3.63	3.64	−1.13	1.28
5	3712.3	4.61	5.30	8.41	−5.38	3.53	19.23	4.61	18.02	8.41	−5.82	3.53

[a] Note: Subscript "i" refers to the vibrational modes 1−5 for K-I, K-II, and K-III. The pressure dependence of the modes is described by a polynomial expansion of the form $\nu_i(P_{\text{ref}}) + \nu'_i(P - P_{\text{ref}}) + \nu''_i(P - P_{\text{ref}})^2$, where ν'_i and ν''_i refers to the first derivative, $\frac{d\nu_i}{dP}$, and second derivative, $\frac{d^2\nu_i}{dP^2}$, respectively. Similarly, the full width at half maxima for each mode (Γ_i) is described by a polynomial expansion of the form $\Gamma_i(P_{\text{ref}}) + \Gamma'_i(P - P_{\text{ref}}) + \Gamma''_i(P - P_{\text{ref}})^2$, where Γ'_i and Γ''_i refers to the first derivative, $\frac{d\Gamma_i}{dP}$, and second derivative, $\frac{d^2\Gamma}{dP^2}$, respectively. The reference pressure, P_{ref}, refers to ambient conditions, i.e., 1 bar or 1×10^{-4} GPa for K-I, P_{ref} refers to ~3.0 GPa for K-II, and P_{ref} refers to ~6.5 GPa for K-III.

three high-energy modes are also often interpreted in terms of independent vibrations of the three "inner surface" hydroxyls.[16,35] For instance, the Oh2-H2 ≈ 0.982 Å is the least hydrogen-bonded owing to the longer Oh2-H2····O4 ~ 3.087 Å and is likely to correspond to the high-energy mode, 3699 cm^{-1} (ν_5). In contrast, Oh4-H4 ≈ 0.975 Å exhibits stronger hydrogen bonding owing to shorter Oh4-H4····O5 ≈ 2.945 Å[14,19] and is likely to correspond to the lower energy mode, 3653 cm^{-1} (ν_2). The hydroxyl bond, Oh3-H3 ≈ 0.976 Å and the Oh3-H3····O3 ≈ 2.980 Å are intermediate between Oh2-H2····O4 and Oh4-

H4····O5, and hence they are likely to correspond to the intermediate energy mode at 3670 cm^{-1} (ν_3). An additional mode (ν_4) is often observed in the Raman spectra of kaolinite.[15,36−38] The clarity of the ν_4 mode is often specific to the kaolinite samples.[15] It is speculated that the ν_4 mode is related to the LO-TO splitting.[15] It is likely that, Oh2-H2····O4 owing to weaker hydrogen bonding, Oh2-H2 is relatively unhinged and exhibits translational motion; thus, ν_5 often shows a shoulder at ν_4 due to the LO-TO splitting.

Hydroxyl Stretching Region at High-Pressures. Upon compression, the crystal structure and the crystallographic environment of proton in kaolinite are affected, which in turn is reflected in the changes observed in the OH-stretching modes of SA and LD kaolinite samples (Figure 3 and Supporting Information, Figure SF7). We have deconvoluted the OH stretching region as a function of pressure (Figure 4 and Supporting Information, Figure SF8). The inner hydroxyl ν_1 mode softens upon compression. The non-linear behavior of the hydroxyl modes ν_i, where i= 1−5, could be well described with a quadratic expansion of the vibrational modes with respect to pressure:

$$\nu_i(P_{\mathrm{ref}}) + \frac{\mathrm{d}\nu_i}{\mathrm{d}P}(P - P_{\mathrm{ref}}) + \frac{\mathrm{d}^2\nu_i}{\mathrm{d}P^2}(P - P_{\mathrm{ref}})^2 \qquad (1)$$

with the inner hydroxyl mode, $\nu_1(P_{\mathrm{ref}}) \approx 3620.1\ (\pm\ 0.05)$ cm^{-1}, $\frac{\mathrm{d}\nu_1}{\mathrm{d}P} \approx -3.16\ (\pm\ 0.11)$ cm^{-1}/GPa, $\frac{\mathrm{d}^2\nu_1}{\mathrm{d}P^2} \approx 0.58\ (\pm\ 0.40)$ cm^{-1}/GPa^2 (Figure 5, Table 2, and Supporting Information, Figure SF9). The reference pressure, P_{ref}, refers to ambient conditions, i.e., 1 bar or 1×10^{-4} GPa. The inner surface hydroxyl groups represented by ν_2 and ν_3 modes also soften upon compression. The non-linear behavior of the ν_2 and ν_3 modes could be well described with the polynomial (1), with $\nu_2(P_{\mathrm{ref}}) \approx 3652.3\ (\pm\ 2.22)$ cm^{-1}, $\frac{\mathrm{d}\nu_2}{\mathrm{d}P} \approx -1.76\ (\pm\ 4.18)$ cm^{-1}/GPa, $\frac{\mathrm{d}^2\nu_2}{\mathrm{d}P^2} \approx -2.86\ (\pm\ 1.33)$ cm^{-1}/GPa^2 and $\nu_3(P_{\mathrm{ref}}) \approx 3669.5\ (\pm\ 2.54)$ cm^{-1}, $\frac{\mathrm{d}\nu_3}{\mathrm{d}P} \approx -7.44\ (\pm\ 3.31)$ cm^{-1}/GPa, $\frac{\mathrm{d}^2\nu_3}{\mathrm{d}P^2} \approx 1.01\ (\pm\ 0.96)$ cm^{-1}/GPa^2 (Figure 5 and Table 2). The inner surface hydroxyl groups ν_5 mode is the least hydrogen-bonded owing to the longer Oh2····O4[19] and shows a weak pressure dependence at low pressures up to ~2.6−3.0 GPa with $\nu_5(P_{\mathrm{ref}}) \sim 3697.9\ (\pm\ 0.70)$ cm^{-1}, $\frac{\mathrm{d}\nu_5}{\mathrm{d}P} \approx -1.74\ (\pm\ 1.15)$ cm^{-1}/GPa, $\frac{\mathrm{d}^2\nu_5}{\mathrm{d}P^2} \approx 0.43\ (\pm\ 0.39)$ cm^{-1}/GPa^2 (Figure 5 and Table 2). The LO-TO ν_4 mode located in the low energy shoulder of the ν_5 mode shows a non-linear pressure dependence, with $\nu_4(P_{\mathrm{ref}}) \approx 3690.2\ (\pm\ 1.48)$ cm^{-1}, $\frac{\mathrm{d}\nu_4}{\mathrm{d}P} \sim -5.21\ (\pm\ 2.40)$ cm^{-1}/GPa, $\frac{\mathrm{d}^2\nu_4}{\mathrm{d}P^2} \sim 1.47\ (\pm\ 0.77)$ (Figure 5 and Table 2). We note that, up to pressures of ~2.9 GPa, all the five modes soften, i.e., $\frac{\mathrm{d}\nu_i}{\mathrm{d}P} < 0$ for i = 1−5 (Figure 5 and Table 2). The pressure dependence of the ν_2 mode $\frac{\mathrm{d}^2\nu_2}{\mathrm{d}P^2} < 0$, i.e., the pressure dependence exhibits local maxima with enhanced softening upon compression. The ν_2 mode is very likely related to the shortest Oh4····O5[19] distance, and it further shortens upon compression, leading to the strengthening of the hydrogen bonding. Similar observations were also made for kaolinite using Fourier transform infrared spectroscopy (FTIR) measurements.[18] Thus, at ~2.9 GPa, the first derivative, i.e., $\frac{\mathrm{d}\nu_i}{\mathrm{d}P}$, transitions from negative, $\left(\frac{\mathrm{d}\nu_i}{\mathrm{d}P}\right) < 0$ to positive, $\left(\frac{\mathrm{d}\nu_i}{\mathrm{d}P}\right) > 0$, where i = 1, 2, and 3 (Figure 5 and Table 2). That is, at pressure < 2.9 GPa, ν_1, ν_2, and ν_3 modes soften upon compression, whereas at pressures >2.9 GPa, all of these modes stiffen. The softening of the OH mode at low pressures is due to the stretching of the O−H distance in the O-H····O unit as the hydrogen bond (H····O) becomes stronger upon compression. In contrast, the stiffening of the OH modes at high pressures are due to shortening of the O−H distances, implying that the hydrogen bonds in the O-H····O units are broken at 2.9 GPa. This is more pronounced for hydroxyl groups that were weakly hydrogen bonded at ambient pressures. Under compression, these weaker hydrogen-bonded O-H····O pairs underwent slight strengthening of hydrogen-bonded interactions till 2.9 GPa, beyond which these pairs showed signs of weakening or snapping of hydrogen bonding. This is very likely due to structural reorganization as kaolinite is compressed. Kaolinite at pressures below 2.9 GPa is referred to as the K-I phase, whereas at pressures greater than 2.9 GPa, it is referred to as the K-II phase. Such transitions in kaolinite and its polymorph dickite have been reported in previous studies (Table 3). Previous studies on single-crystal dickite using Raman spectroscopy revealed a transition from dickite to its high-pressure polymorph at pressures between ~2.0 and 2.5 GPa.[39] The transition pressures of around ~2.0 GPa was further confirmed by X-ray diffraction studies.[20] The transition in dickite was associated with a 2% reduction in the unit cell volume.[20] Similar to the transition of dickite to the high-pressure polymorph of dickite, X-ray diffraction studies of kaolinite showed a transition from low-pressure kaolinite (K-I) to an intermediate pressure phase of kaolinite (K-II) between 3.4 and 3.9 GPa.[17]

Table 3. Polytypic Transition and Pressure-Induced Hydration in Layered Hydrous Silicates Including Kaolinite Polymorphs and Talc[a]

	P_{tr} [GPa]	temperature [°C]	method
	1:1 Clays (Tet-Oct···Tet-Oct)		
dickite → high P dickite	2.0−2.5	25	Raman[39]
dickite → high P dickite	2	25	SCXRD[20]
kaolinite (KI → KII)	3.4−3.9	25	PXRD[17]
kaolinite (KI → KII)	3.7	25	FTIR[18]
kaolinite (KII → KIII)	6.5−7.2	25	PXRD[17]
kaolinite (KII → KIII)	7	25	FTIR[18]
kaolinite (KI → KII)	2.9	25	Raman[$]
kaolinite (KII)*	~3.7−3.9	25	Raman[$]
kaolinite (KII → KIII)	6.1	25	Raman[$]
kaolinite, KII → SuHy (PIH)	2.6	200	PXRD, IR[21]
nacrite → PIH	3	200	PXRD, IR[22]
	2:1 Clays (Tet-Oct-Tet···Tet-Oct-Tet)		
talc (talc-I → talc-II)	4	25	PXRD[61]
talc (talc-I → talc-II)	4	425	PXRD[61]
talc (talc-II → 10 Å)	4	27	PXRD[59]
Na-hectorite → PIH	1.7	25	PXRD[60]
	2:1 Clays (Tet-Oct-Tet···O···Tet-Oct-Tet)		
smectites → PIH	ambient	25	PXRD[72]

[a] Raman: Raman Spectroscopy; SCXRD: single-crystal X-ray diffraction; PXRD: powder X-ray diffraction; FTIR: Fourier transform infrared spectroscopy; SuHy: super-hydrated kaolinite; PIH: pressure-induced hydration; ($): this study; (*): refer to Figure 5; O: cation.

Table 4. Pressure and Temperature Conditions Explored in Each Experiment[a,b]

serial #	experiment #	$(T_{\text{in}}, P_{\text{in}})$	$(T_{\text{int}}, P_{\text{int}})$	$(T_{\text{max}}, P_{\text{max}})$	$(T_{\text{fin}}, P_{\text{fin}})$	10 Å phase
1	HPT-1	22, 0.3	22, 3.5	225, 4.1	22, 1.8	yes
2	HTP-2	22, 0.3	220, 3.5	220, 4.6	22, 2.3	yes
3	HTP-3	22, 0.1	350, 2.1	350, 2.1	22, 0.2	no
4	HTP-4	22, 0.8	22, 0.9	225, 3.1	22, 1.7	no
5	HTP-5	22, 0.3	200, 1.6	200, 3.7	22, 1.7	no
6	HTP-6	22, 0.2	22, 1.1	220, 5.1	22, 2.2	yes

[a] Note: Subscript “in” refers to initial P−T conditions, subscript “int” refers to the intermediate P, T conditions, subscript “max” refers to the maximum P, T conditions explored, and subscript “fin” refers to the final P, T conditions after the experiment. The “final” pressure need not be the same as the “initial” pressure; it is often dependent on the P−T path explored. In the HPT-1 experiment, the pressure was increased initially to the ice phase. This was followed by an increase in temperature. For the HTP-*n* ($n = 2{-}6$) experiments, the P−T conditions remain in the liquid water phase. [b] Temperatures and pressures are reported in °C and GPa, respectively.

In our study, in contrast to the ν_2 mode, the ν_5 mode, which is likely to be associated with the longer Oh2···O4,[19] i.e., weak or no hydrogen bonding, softens the least with $\frac{d\nu_5}{dP} \approx -1.74$ ($\pm$ 1.15) cm^{-1}/GPa (Table 2). At ~2.9 GPa, we note that the ν_5 mode stiffens discontinuously, $\Delta\nu_5 \approx +6.7$ cm^{-1} (Figure 5). The ν_4 mode also shows discontinuous stiffening at 2.9 GPa, but the magnitude of the stiffening is lower than that of the ν_5 mode, with $\Delta\nu_4 \approx 4.4$ cm^{-1} (Figure 5). At pressures > 2. 9 GPa, i.e., following the discontinuous stiffening, both ν_5 and ν_4 modes exhibit a non-linear behavior, i.e., they first soften till pressures of 4 GPa, and upon further compression beyond 4 GPa, they stiffen. Thus, the K-II region in our study shows a distinct behavior for modes, $\left(\frac{d\nu_i}{dP}\right) > 0$, where $i = 1$, 2, and 3, but for $i = 4$ and 5, $\left(\frac{d\nu_i}{dP}\right) < 0$ up to pressures of 4 GPa, but $\left(\frac{d\nu_i}{dP}\right) > 0$ at pressures beyond 4 GPa. This might imply that, at the KI-KII transition at 2.9 GPa, most hydrogen bonds snap, but for the ν_4 and ν_5 modes, the hydrogen bonds initially break and then again form with newer oxygen atoms in the adjacent layers. This newly formed hydrogen bond strengthens till 4 GPa, beyond which it breaks, exhibiting the non-linear behavior of the ν_4 and ν_5 modes.

Upon further compression, X-ray diffraction studies of kaolinite showed another transition from the intermediate pressure kaolinite (K-II) to a high-pressure kaolinite between 6.5 and 7.2 GPa.[17] High-pressure FTIR study on kaolinite also exhibited the K-I to K-II transition and K-II to K-III transition at 3.7 and 6.1 GPa, respectively.[17] Based on our results, we also note a transition in the pressure dependence of the hydroxyl modes at around 6.1 GPa and we denote this as the transition from the K-II to K-III phase (Figure 5 and Table 2).

It is known that the stacking of the second layer of Tet-Oct over the first Tet-Oct layer could be achieved either by a rotation of the second layer over the first layer, with the rotation amount being $k\frac{\pi}{3}$, where $k = 0{-}6$, i.e., six distinct rotations of 0° to 360° in increments of 60°, or by translation. Six distinct translations have been identified: 0, $\frac{\boldsymbol{a}}{3}$, $\frac{\boldsymbol{b}}{3}$, $\frac{2\boldsymbol{a}+\boldsymbol{b}}{3}$, $\frac{\boldsymbol{a}+2\boldsymbol{b}}{3}$, and $\frac{2(\boldsymbol{a}+\boldsymbol{b})}{3}$ (where $\boldsymbol{a}$ and $\boldsymbol{b}$ are lattice vectors in the $a{-}b$ plane). With these six rotations and six translations, a total of 36 combinations are possible.[40] These rotations and translations tend to affect the energetics due to a combination of (*a*) repulsive interaction between Al cations of the octahedral units of the first layer with the Si cation of the tetrahedral units of the overlying second layer and (*b*) an attractive interaction between the O−H units, i.e., inner surface hydroxyl of the first layer with the basal oxygen anions of the tetrahedral units of the overlying or the second layer.[40] Recent first-principles simulations of kaolinite polymorphs have investigated the relative energetics of all the abovementioned 36 polymorphs that results from the combination of rotation and translation.[41,42] Using the converged results of the crystal structure, the high-pressure X-ray diffraction results for the K-II phase was identified as a polymorph in which the second layer was translated with respect to the first layer by a translation vector $\frac{2\boldsymbol{a}+\boldsymbol{b}}{3}$ without any rotation of the second layer, i.e., $k = 0$.[17]

As kaolinite undergoes a transition from the K-I to K-II phase, the adjacent Tet-Oct layers are offset by a translation vector $\frac{2\boldsymbol{a}+\boldsymbol{b}}{3}$. This causes snapping of the weaker hydrogen bonds as we notice from the abrupt shift in the ν_5 and the ν_4 modes, which are related to the longer Oh2···O(4) pairs. Meanwhile, the relatively stronger hydrogen bonds are likely to weaken, thus indicating a transition from $\left(\frac{d\nu_i}{dP}\right) < 0$ to positive, $\left(\frac{d\nu_i}{dP}\right) > 0$, where $i = 1$, 2, and 3. We note that this transition occurs at slightly lower pressures of ~2.9 GPa compared to 3.4−3.9 GPa from a previous study.[18] This discrepancy may be attributed to two factors: (a) sample crystallinity and (b) the different experimental probe. While, in our study, we have used kaolinite samples that are with high Hinckley indices (H_i), Keokuk kaolinite, one of the most ordered kaolinite, was used in prior study.[18] The slight variation of the Al−Si ordering might lead to changes in the repulsive interaction between the Al cation and the overlying Si cation and attractive interaction between the inner surface hydroxyl and the overlying oxygen anion of the tetrahedral layer. The slight variation in the energetics due to Al−Si order−disorder is the likely cause for the observed differences in the transition pressures between the samples explored in this study and those explored in earlier studies.[18] The slight mismatch in transition pressure may in part be attributed to the differences in the probes used in the previous measurements (XRD)[17] with the present study (Raman spectroscopy). While XRD examines changes that are averaged over the bulk of the sample, Raman spectroscopy detects changes in the local structure, which may initiate at a lower pressure.[43,44] This is consistent with our Raman results, where we observe the initiation of the transition occurs at 2.9 GPa.

Kaolinite and Water Interaction at High Pressures and Temperatures. To examine the interaction of water with kaolinite and possible intercalation of water in the interlayer region of kaolinite at high pressures and temperatures, we loaded kaolinite and water in hydrothermal diamond anvil cell.[28,45,46] Before the initiation of the high PT experiment, we collected reference Raman spectra for the hydroxyl stretching modes for

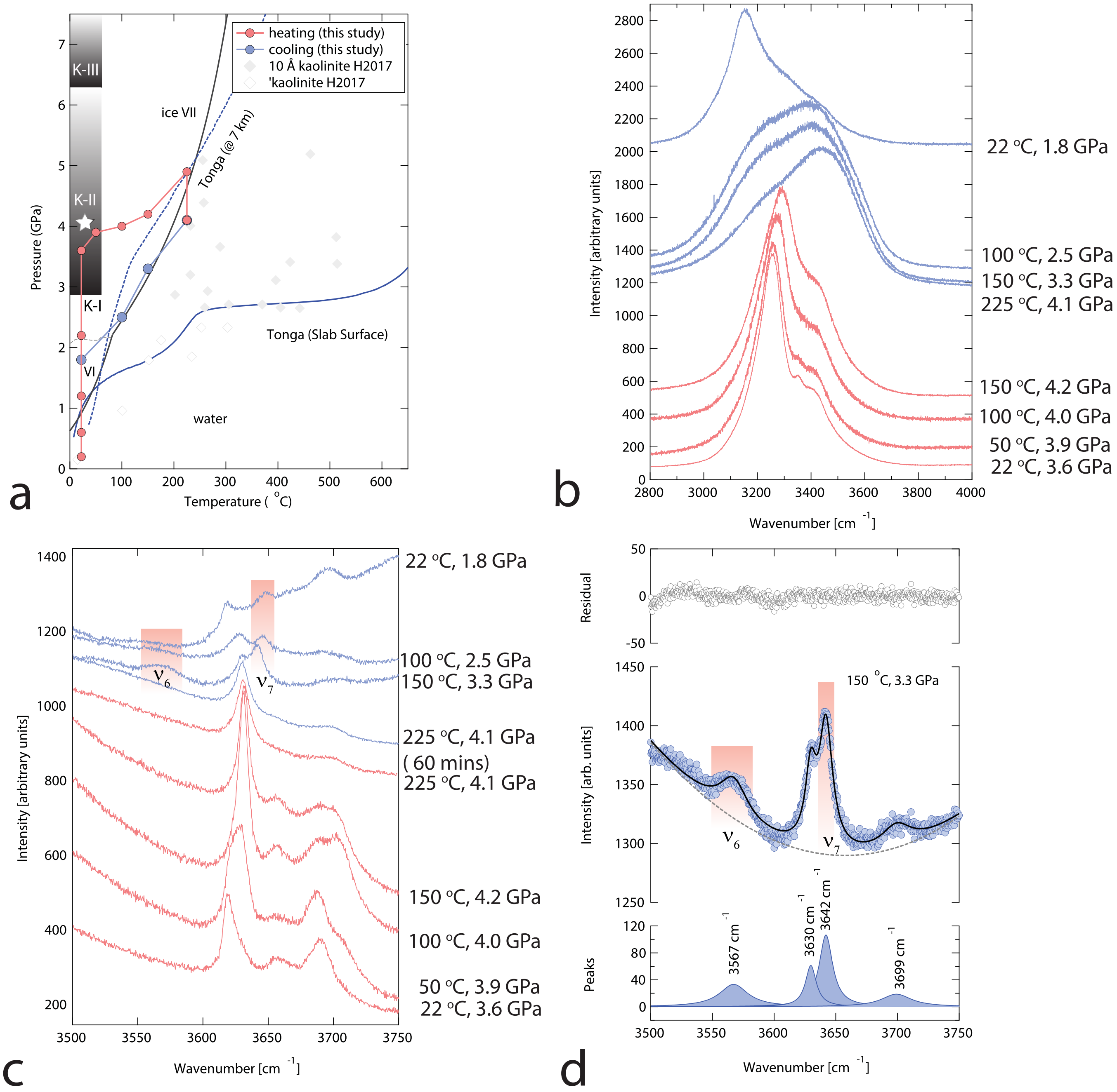

Figure 6. (a) Plot shows P−T path adopted for the kaolinite−water experiment (HPT-1). The red filled symbols and line show the initial pressurization path for "kaolinite + H_2O" via the ice-VI and ice-VII phase. Following the initial compression, the "kaolinite + H_2O" sample was heated such that ice-VII transitions into liquid water. At $T_{max} \approx 225$ °C, and $P_{max} \approx 4.1$ GPa, the "kaolinite + H_2O" sample was held for >60 min. Then, the "kaolinite + H_2O" sample was cooled down to $T_{fin} \approx 22$ °C, and the sample decompressed to a final pressure, $P_{fin} \approx 1.8$ GPa (Table 4). The cooling path is shown in blue filled symbols and line. The geothermal gradient along the Tonga subduction zone is also shown at the slab surface (blue line), inside the slab at Moho depth (dashed blue line). The P−T boundary for kaolinite (white rhombus), "super-hydrated" 10 Å kaolinite (filled gray rhombus), from a recent study (H2017)[21] is also shown. (b) Plot shows Raman spectra for ice-VI, ice-VII, and liquid water in the 3000−4000 cm^{-1} region along the P−T paths in (a). (c) Plot shows Raman spectra for kaolinite in the hydroxyl region, i.e., 3000−4000 cm^{-1}, along the P−T paths in (a). The red color refers to the initial compression followed by heating as in (a), whereas the blue color represents the cooling path as shown in (a). (d) Deconvolution of the Raman spectra for kaolinite at 150 °C and 3.3 GPa. We note the additional peak at 3567 cm^{-1}, which is likely to be associated with the interlayer water in 10 Å kaolinite.[21] A similar peak is also observed in halloysite.[71]

both pure water and LD kaolinite samples inside the sample chamber (Supporting Information, Figure SF10). The frequency region between 2800 and 4000 cm^{-1} of the pure water Raman spectrum is dominated by three distinct bands at 3225, 3436, and 3610. This is in good agreement with the reported Raman spectra for liquid water[47−49] and is due to the overtone of the bending mode and symmetric and asymmetric stretching vibrations. The OH-stretching frequencies for the LD kaolinite sample consisted of four distinct modes at ~3620 cm^{-1} (ν_1), 3648 cm^{-1} (ν_2), 3691 cm^{-1} (ν_4), and 3699 cm^{-1} (ν_5).

We explored distinct pressure and temperature paths to examine the kaolinite and water interaction. We categorized our

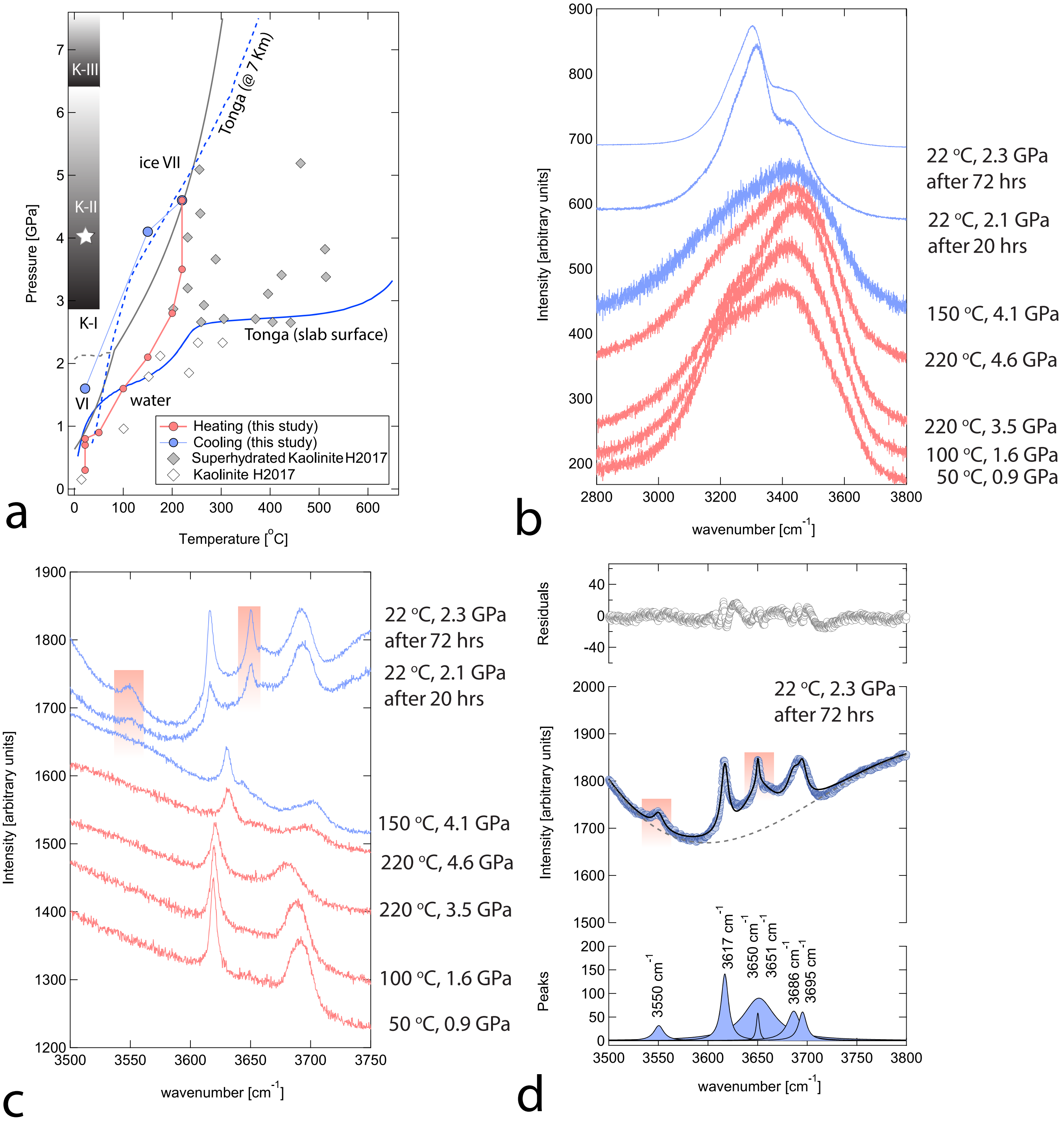

Figure 7. (a) Plot shows the P−T path adopted for the kaolinite−water experiment (HTP-2). The red filled symbols and line show the initial heating and pressurization path for "kaolinite + H_2O", which lies along the liquid water region. At $T_{max} \approx 220$ °C and $P_{max} \approx 4.6$ GPa, i.e., at the P−T boundary of liquid water and ice-VII phase, the "kaolinite + H_2O" sample was held for >60 min. Then, the "kaolinite + H_2O" sample was cooled down to $T_{fin} \approx 22$ °C, and the sample decompressed to a final pressure P_{fin} of ∼2.3 GPa (Table 4). The cooling path is shown in blue filled symbols and line. The geothermal gradient along the Tonga subduction zone is also shown at the slab surface (blue line), inside the slab at Moho depth (dashed blue line). The P−T boundary for kaolinite (white rhombus), "super-hydrated" 10 Å kaolinite (filled gray rhombs), from a recent study (H2017)[21] is also shown. (b) Plot shows Raman spectra for liquid water in the 3000−4000 cm^{-1} region along the P−T paths in (a). (c) Plot shows Raman spectra for kaolinite in the hydroxyl region, i.e., 3000−4000 cm^{-1}, along the P−T paths in (a). The red color refers to the initial compression followed by heating as in (a), whereas the blue color represents the cooling path as shown in (a). (d) Deconvolution of the Raman spectra for the super-hydrated kaolinite sample collected after 72 h at 22 °C and 2.2 GPa. In addition, the peak at 3650 cm^{-1} is sharp and intense and is also indicative of super-hydrated kaolinite.

experiments into two distinct pressure−temperature paths. In the first set of experiments, labeled HPT-*n* (where *n* is the experiment run #, Table 4), "kaolinite + H_2O" was first compressed to an intermediate (int) pressure, P_{int}, at 22 °C (292 K) above the water−ice VI phase boundary. Then, "kaolinite + H_2O" was heated to the maximum temperature T_{max} and the pressure increased to P_{max}. This was followed by cooling to the final temperature of T_{fin}. Upon cooling back to the final

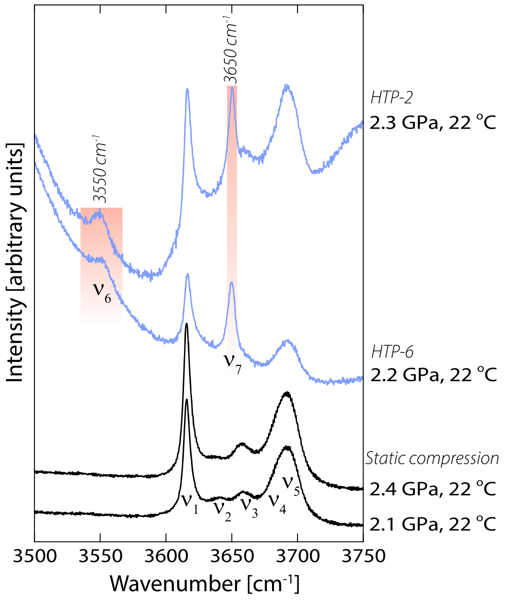

Figure 8. Plot of hydroxyl stretching modes of LD kaolinite in the range from 3500 to 3750 cm^{-1}. The Raman spectra for static compression at 2.1 and 2.4 GPa and 22 °C are shown in black. The Raman spectra from HDAC run HTP-2 and HTP-6 (Table 4) are shown in blue. The ν_6 mode ($\sim$3550 cm^{-1}) is a new mode associated with the intercalation of water in the interlayer region of kaolinite. The ν_7 mode ($\sim$3650 cm^{-1}) observed in the HTP-2 and HTP-6 is distinct from the ν_2 and ν_3 modes observed from static compression at 2.1 and 2.4 GPa and appear in between the two modes.

temperature T_{fin} $\approx$22 °C (292 K), "kaolinite + H_2O" decompressed back to P_{fin}, where P_{fin} is often greater than the initial (in) pressure, P_{in}. Compressing the sample before heating allows us to compare our results directly with a prior study.[21] For instance, in HPT-1, we first increased the pressure at ambient temperature, i.e., upon compression, the water transformed to ice-VI at ~1 GPa and then to ice-VII at ~2 GPa. The Raman spectra in the 2800−4000 cm^{-1} region reveal the ice-VII phase, in agreement with previous studies.[47−49] At room temperature and 3.5 GPa (P_{int}), we find OH-stretching modes at 3619, 3626, 3658, 3680, and 3690 cm^{-1}. Upon reaching a pressure of 3.5 GPa, i.e., in the K-II phase, we heated the kaolinite and H_2O (ice-VII) (Figure 6 and Table 4). We heated the cell to 225 °C (T_{max}) in an incremental step of 50 °C. We collected the Raman spectra at each of these temperatures. At the temperature of 225 °C and pressure of ~4.1 GPa (P_{max}), we heated the cell for more than an hour (>60 min). At 225 °C, we observed modes at ~3630 and 3698 cm^{-1}. In addition, we noticed a severe broadening of the 3698 cm^{-1} mode. This is very likely due to the stacking disorder and a subsequent weakening of the interlayer hydrogen bonding in kaolinite tetrahedral-octahedral-tetrahedral (T-O-T) layers. On cooling down to ~150 °C and concomitant reduction in pressures to ~3.3 GPa, we observe two new modes near ~3550 cm^{-1} (ν_6) and 3640 cm^{-1} (ν_7). Upon further reduction in temperature to 22 °C (T_{fin}) and simultaneous reduction of pressures to ~1.8 GPa (P_{fin}), we note that the full width at half maxima of the ν_6 mode becomes broader. In contrast, at 22 °C (T_{fin}) and 1.8 GPa (P_{fin}), the ν_7 mode becomes more intense and is still distinct from the ν_2 and ν_3 modes of kaolinite.

In the second set of experiments, labeled HTP-*n* (where *n* is the experiment run #, Table 4), the initial temperature (T_{in}) for "kaolinite + H_2O" is room temperature (~22 °C), but the initial pressure (P_{in}) is always below the water-ice-VI phase boundary. "Kaolinite + H_2O" was first heated to an intermediate temperature T_{int}. This heating leads to compression and the pressures changes to P_{int} such that the assemblage is at P_{int}, T_{int}, where liquid water is the thermodynamically stable phase. Then, "kaolinite + H_2O" was compressed to the maximum pressure P_{max}. This was followed by cooling to the final temperature of T_{fin}. Upon cooling to T_{fin}, "kaolinite + H_2O" decompressed to P_{fin}, where $P_{fin} > P_{in}$. For instance, in the experiment, HTP-2, we began at initial pressures of 0.3 GPa (P_{in}) and ambient temperature of 22 °C (T_{in}), i.e., in the liquid water phase. Then, we heated the sample to 220 °C (T_{max}), this led to concurrent changes in the pressures ~3.5 GPa (P_{int}). The maximum pressures and temperatures explored were ~4.5 GPa (P_{max}) and 200 °C (T_{max}). The HDAC was held for more than an hour (>60 min) at the P_{max} and T_{max} conditions. Upon cooling, similar to the HPT-1, we observed the appearance of two new modes near ~3550 cm^{-1} (ν_6) and 3650 cm^{-1} (ν_7). We note that ν_7 is distinct from both ν_2 and ν_3 hydroxyl stretching modes of kaolinite. The ν_7 mode frequency is in between ν_2 and ν_3 modes. Additionally, the full width at half maxima value for ν_7 is an order of magnitude smaller than ν_2 and ν_3 modes, likely indicating toward a different origin of the ν_7 mode (Figures 7 and 8 and Supporting Information, Table ST1). These two modes (ν_6 and ν_7) are indicative of the formation of the super-hydrated phase. We collected the Raman spectrum of the super-hydrated phase on the cooling cycle to room temperature (T_{fin}) and a pressure of ~2.1 GPa (P_{fin}) and noted that the ν_6 mode becomes more intense at a lower temperature. We collected Raman spectra again after an interval of ~20 h and observed that the ν_6 and ν_7 modes grew more intense with time (Figure 7). We always observed the ν_6 mode upon cooling, but so far, we have not been able to detect ν_6 at the maximum temperatures explored. It is very likely that, at the higher temperatures, the interlayer water molecules are more disordered, resulting in a broader full width at half maxima for the ν_6 mode, making it harder to detect. Upon cooling down to lower temperatures but retaining high pressures might lead to the ordering of the intercalated water in the interlayer region and provide better Raman scattering cross section, resulting in a well-defined and intense mode (Supporting Information, Figure SF12). We have repeated the high-pressure and temperature experiments and have consistently observed the intercalation of water and the presence of modes ν_6 and ν_7 in super-hydrated kaolinite when the maximum pressure (P_{max}) explored were >4 GPa (Table 4) i.e., P_{max} > 2.9 GPa, i.e., P_{tr} for K-I to K-II. One possible explanation might be that, upon the K-I to K-II transition, even though all the hydrogen bonds are broken, we note a non-linear behavior for the ν_4 and ν_5 modes in the K-II region (Figure 5 and Table 3). It is likely that, at P_{tr} (2.9 GPa), the hydrogen-bonded pairs O-H···O for the ν_4 and ν_5 modes are snapped and then new hydrogen-bonded pairs O-H···O form with newer oxygen atoms in the adjacent layers. This newly formed hydrogen bond strengthens till ~4 GPa and very likely weakens beyond this pressure when the intercalation of water molecules in the interlayer region is facilitated. The intercalation is always associated with the formation of ~3550 cm^{-1} (ν_6) and 3650 cm^{-1} (ν_7) modes. However, in some experiments where the maximum pressure (P_{max}) did not exceed 4 GPa, we were not able to confirm the intercalation of water, i.e., upon cooling, we did not observe the formation of ν_6 and ν_7 modes. Thus, for the high-pressure and temperature-induced intercalation of water in the interlayer region, it is crucial that kaolinite and water react at pressures that are well within the K-II phase stability, i.e., pressures exceeding 4 GPa where the minima are observed for the pressure dependence of the ν_4 and ν_5 modes (Figure 5). As the interlayer hydrogen bonds are weaker in the K-II phase, it acts as a precursor for the super-hydrated kaolinite.

Recent X-ray diffraction and FTIR study[21] on kaolinite shows the formation of the super-hydrated phase at a slightly lower pressure (∼2.7 GPa) than that observed in the present study. It is likely the pressure−temperature path followed in the hydration experiments plays a major role in the intercalation pressure−temperature values. We have followed two pressure−temperature paths during the hydration experiments: (1) initial compression through the ice phase and then heating (HPT-*n*) (Figure 6 and Table 4) and (2) initial heating through the water phase and then compression (HTP-*n*) (Figure 7 and Table 4). It is very likely that the KI-KII transition pressure (P_{tr}) is affected (lowered) if the sample is first compressed, i.e., liquid water to ice-VI/VII may contribute to quasi-hydrostatic conditions and may lead to KI-KII polytypic transitions at slightly lower pressures, resulting in the formation of the super-hydrated phase at a lower pressure.

■ DISCUSSIONS

Pressure-induced hydration in minerals is a unique phenomenon where the volume of mineral expands upon compression as it accommodates water molecules at higher pressures. This phenomenon has been extensively investigated for the zeolites group of minerals with crystal structures consisting of a tetrahedral framework of aluminum and silicon ions.[50] The accommodation of foreign molecules including water molecules within the cages of the tetrahedral framework is often accommodated by tilts and rotation of the tetrahedral framework, thus creating enhanced cages. In stark contrast with the zeolites, clays have a layered structure. Upon compression, the compressibility across the clay layer is often significantly greater than along the layers. This is documented with a pressure-induced sharp decrease in the *c*/*a* ratio and also in anisotropic linear elastic moduli and their pressure dependence, i.e., $K_{[001]} > K_{[100]} \approx K_{[010]}$.[17,51−54] Thus, upon compression, the interlayer region of clays undergoes compression at a faster rate compared to the compression along [100] and [010] directions. The coefficients of thermal expansions (α) for layered silicates are also quite anisotropic, with $\alpha_{[001]} > \alpha_{[100]} \approx \alpha_{[010]}$.[19,55−57] However, thermal expansion is $\sim 10^{-5}$/K and would translate to very little expansion within the thermodynamic stability range of most clays, i.e., 500−800 K. Thus, based on the anisotropic thermoelasticity of clays, one would expect such insertion of water molecules at high pressures to be counterintuitive. This makes the pressure-induced hydration in clays quite counterintuitive and is indeed a unique phenomenon. Such pressure-induced hydration in the interlayer region of 2:1 clays has been documented in talc [$Mg_3Si_4O_{10}(OH)_2$][58,59] and more recently in synthetic Na-fluorohectorite clays.[60] For instance, at pressures of ∼6.5 GPa and temperatures of ∼550 °C, in the talc + water system, talc transforms to a 10 Å phase, where water molecules are intercalated in interlayer space between the tetrahedral-octahedral-tetrahedral (T-O-T) layers.[58] In talc, the T-O-T layers are held together by weak van der Waals interactions. Recent investigations have indicated that talc also undergoes a pressure-induced transformation from talc-I to talc-II at around 4 GPa.[61] This is further confirmed by in situ X-ray-based observations, which have concluded that talc-II is stable between 4 and 9 GPa, i.e., corresponding to a depth of 125−275 km.[59] It is suggested that the talc-II phase, which is stable at 4 GPa, is the likely precursor to the 10 Å phase in the water-saturated system.[59,61]

Based on our study, it is apparent that kaolinite undergoes a pressure-induced transformation at ∼2.9 GPa from K-I to K-II, which translates to an ∼90 km depth in a typical subduction zone. The transition is associated with the breaking of hydrogen bonds formed by the inner surface hydroxyls and a reorganization of the Tet-Oct···Tet-Oct stacking.[17,20] However, at pressures beyond 2.9 GPa, new hydrogen bonds are formed, and they are first strengthened and then weakened at further higher pressures (∼4 GPa) as evidenced by the non-linear behavior of both ν_4 and ν_5 modes. It is likely that the K-II phase with broken hydrogen bonds in the interlayer region is primed ready for the insertion/accommodation of the water molecules. In our experiments that are conducted in water-saturated conditions, the K-II phase transforms to the newly super-hydrated kaolinite at ∼4 GPa (Figures 6 and 7), i.e., ∼ 120 km depth in a typical subduction zone. The weakened hydrogen bonding in the interlayer region is associated with the K-I to K-II transition in kaolinite, which leads to the modification of O-H···O bonding to O-H····X bonding where X refers to an intercalated species.[62] In the present case, X is likely the oxygen ion of the intercalated water molecules (H_2O). To understand the effect of temperature on the super-hydrated phase, we heated it to 100 °C and found that, upon heating, the ν_6 mode became less intense and the full width at half maxima (FWHM) significantly increases such that we were unable to detect the mode. However, upon cooling down, the intensity of the ν_6 mode recovered. This indicates that the temperature affects the structure and configuration of the water molecules in the interlayer region. At high temperatures, the water molecules in the interlayer region are likely to be more disordered, resulting in the less intense ν_6 mode that also has a larger FWHM. This might also explain why it is often difficult to detect this mode at the highest pressures and temperatures and becomes sharper and more intense upon cooling. The ν_7 mode remained intense upon heating up to ∼100 °C. To explore the effects of pressure, we also compressed the super-hydrated phase. Upon compression, we noticed softening of the ν_6 mode with $\frac{d\nu_6}{dP} \approx -6.8 \pm 1.1$ cm^{-1}/GPa and minor stiffening of the ν_7 mode with $\frac{d\nu_7}{dP} \approx 0.8 \pm 0.1$ cm^{-1}/GPa (Supporting Information, Figure SF12). The softening of the ν_6 mode is likely due to the enhancement of the hydrogen bonding between the water molecules (H_2O) in the interlayer region and the oxygen atoms of the octahedral (O_O) and tetrahedral (O_T) layer that sandwiches the interlayer region, i.e., $H_2O \cdots O_T$ or $H_2O \cdots O_O$. It is also likely that hydrogen bonding between the water molecules in the interlayer region, i.e., $H_2O \cdots OH_2$, also strengthens upon compression and weaken upon heating.

Hydrous phases that are thermodynamically stable in the subducting slab play a vital role in transporting water into the deep Earth. Most of the hydrous phases that are abundant in the subducting lithosphere often belong to the simplified ternary MgO-SiO_2-H_2O (MSH) system representing hydrated peridotite.[9] Effective water transport is facilitated if the P−T path of the slab continuously coincides with the P−T stability field of these hydrous phases in the P−T space. However, gaps in the P−T stability field of hydrous phases are known from experimental studies, i.e., the P−T stability field of serpentine ($Mg_3Si_2O_5(OH)_4$) and that of high-pressure phase-A

($Mg_7Si_2O_8(OH)_6$) do not fully overlap such that the P−T paths of subducting slabs pass through P−T regions where no hydrous phases are stable (choke point); thus, the effective mechanism of water transport to the deep interior is severely affected.[9] The 10 Å phase in MSH ternary has stability between 4 and 9 GPa, i.e., 125−275 km, and effectively bridges the P−T gap and provides an effective mechanism of continuous transport of water.[58,59,61] However, it is well known that aluminous hydrous phases often have higher thermal stability than the alumina-free hydrous phase.[63] Our experiments show that the super-hydrated kaolinite phase is also likely to be stable at around 4 GPa, i.e., close to the thermodynamic choke point, and is likely to alleviate this issue by providing an additional mechanism of water transport to the deep Earth. Further study on the high-temperature stability of super-hydrated kaolinite would shed valuable insight into the transport of water into the deep Earth.

In addition to water, it is possible that kaolinite or other clays might also play a vital role in sequestering carbon and nitrogen in subduction zone settings. Layered silicates are known to host the methane molecule (CH_4) in the interlayer region of layered silicates and could potentially sequester both carbon and hydrogen.[64] Under hydrothermal conditions, kaolinite could react with ammonium hydroxide and intercalate ammonium (NH_4^+) in the interlayer region, thus transforming to tobelite.[65] Thus, kaolinite with intercalated ammonium and other ammonium-bearing layered silicates could play a vital role in sequestering nitrogen and hydrogen in the deep Earth and account for the nitrogen deficit in the bulk silicate Earth.[66−68] Moreover, such intercalation of methane and or ammonium may also affect the stability of the super-hydrated phase.

At higher pressures (~6.1 GPa), the K-II phase eventually transforms to the K-III phase (Figure 5), and K-III eventually decomposes to phase-pi ($Al_3Si_2O_7(OH)_3$) at ~7 GPa.[21,69,70] This transformation is likely to be associated with the release of aqueous fluids and might contribute to dehydration-related seismicity. Similarly, at higher temperatures, the super-hydrated phase is also likely to dehydrate, which would release aqueous fluids and might induce subduction zone seismicity. The dehydration kinetics of the super-hydrated phase needs to be characterized to gain a better insight into the dehydration-induced seismicity in subduction zone settings.

■ ASSOCIATED CONTENT

Supporting Information

The Supporting Information is available free of charge at https://pubs.acs.org/doi/10.1021/acsearthspacechem.0c00349.

Effect of laser power on kaolinite samples and additional figures and tables (Figures SF1−SF12 and Table ST1) (PDF)

■ AUTHOR INFORMATION

Corresponding Author

Abhisek Basu − *Earth Materials Laboratory, Department of Earth, Ocean and Atmospheric Science, Florida State University, Tallahassee, Florida 32306, United States;* orcid.org/0000-0002-0283-1778; Email: abasu@fsu.edu

Author

Mainak Mookherjee − *Earth Materials Laboratory, Department of Earth, Ocean and Atmospheric Science, Florida State University, Tallahassee, Florida 32306, United States;* orcid.org/0000-0002-0605-5964

Complete contact information is available at: https://pubs.acs.org/10.1021/acsearthspacechem.0c00349

Notes

The authors declare no competing financial interest.

■ ACKNOWLEDGMENTS

The authors thank the two anonymous reviewers for their constructive comments that enhanced the clarity of the manuscript. The authors acknowledge support from the National Science Foundation (EAR1638752 and EAR1753125). A.B. acknowledges funding for the Dean's post-doctoral fellowship from the College of Arts and Sciences, Florida State University.

■ REFERENCES

(1) Garrels, R. M.; MacKenzie, F. T. *Evolution of Sedimentary Rocks*; W. W. Norton & Co.: New York, 1971.

(2) Bodnar, R. J.; Azbej, T.; Becker, S. P.; Cannatelli, C.; Fall, A.; Severs, M. J. Whole Earth Geohydrologic Cycle, from the Clouds to the Core: The Distribution of Water in the Dynamic Earth System. In *The Web of Geological Sciences: Advances, Impacts, and Interactions*; Geological Society of America, 2013; Vol. *500*, pp. 431−461, DOI: 10.1130/2013.2500(13).

(3) Syvitski, J. P. M.; Peckham, S. D.; Hilberman, R.; Mulder, T. Predicting the Terrestrial Flux of Sediment to the Global Ocean: A Planetary Perspective. *Sediment. Geol.* **2003**, *162*, 5−24.

(4) Widom, H. L. Lithogenous Materials in Marine Sediments. In *Chemical Oceanography*; Riley, J. P., Chester, R., Eds.; Academic Press, 1976; pp. 103−135.

(5) Weaver, C. E. Clays, Muds, and Shales. In *Developments in Sedimentology*; Elsevier, 1989; p 310.

(6) Plank, T.; Langmuir, C. H. Tracing Trace Elements from Sediment Input to Volcanic Output at Subduction Zones. *Nature* **1993**, *362*, 739−743.

(7) Rea, D. K.; Ruff, L. J. Composition and Mass Flux of Sediment Entering the World's Subduction Zones: Implications for Global Sediment Budgets, Great Earthquakes, and Volcanism. *Earth Planet. Sci. Lett.* **1996**, *140*, 1−12.

(8) Peacock, S. M. Fluid Processes in Subduction Zones. *Science* **1990**, *248*, 329−337.

(9) Kawamoto, T. Hydrous Phases and Water Transport in the Subducting Slab. *Rev. Mineral. Geochem.* **2006**, *62*, 273−289.

(10) Ono, S. Stability Limits of Hydrous Minerals in Sediment and Mid-Ocean Ridge Basalt Compositions: Implications for Water Transport in Subduction Zones. *J. Geophys. Res. Solid Earth* **1998**, *103*, 18253−18267.

(11) Balan, E.; Saitta, A. M.; Mauri, F.; Calas, G. First-Principles Modeling of the Infrared Spectrum of Kaolinite. *Am. Mineral.* **2001**, *86*, 1321−1330.

(12) Balan, E.; Lazzeri, M.; Saitta, A. M.; Allard, T.; Fuchs, Y.; Mauri, F. First-Principles Study of OH-Stretching Modes in Kaolinite, Dickite, and Nacrite. *Am. Mineral.* **2005**, *90*, 50−60.

(13) Balan, E.; Delattre, S.; Guillaumet, M.; Salje, E. K. H. Low-Temperature Infrared Spectroscopic Study of OH-Stretching Modes in Kaolinite and Dickite. *Am. Mineral.* **2010**, *95*, 1257−1266.

(14) Bish, D. L. Rietveld Refinement of the Kaolinite Structure at 1.5 K. *Clays Clay Miner.* **1993**, *41*, 738−744.

(15) Johnston, C. T.; Sposito, G.; Birge, R. R. Raman Spectroscopic Study of Kaolinite in Aqueous Suspension. *Clays Clay Miner.* **1985**, *33*, 483−489.

(16) Johnston, C. T.; Kogel, J. E.; Bish, D. L.; Kogure, T.; Murray, H. H. Low-Temperature FTIR Study of Kaolin-Group Minerals. *Clays Clay Miner.* **2008**, *56*, 470−485.

(17) Welch, M. D.; Crichton, W. A. Pressure-Induced Transformations in Kaolinite. *Am. Mineral.* **2010**, *95*, 651−654.

(18) Welch, M. D.; Montgomery, W.; Balan, E.; Lerch, P. Insights into the High-Pressure Behavior of Kaolinite from Infrared Spectroscopy and Quantum-Mechanical Calculations. *Phys. Chem. Miner.* **2012**, *39*, 143−151.

(19) Bish, D. L.; Johnston, C. T. Rietveld Refinement and Fourier-Transform Infrared Spectroscopic Study of the Dickite Structure at Low Temperature. *Clays Clay Miner.* **1993**, *41*, 297−304.

(20) Dera, P.; Prewitt, C. T.; Japel, S.; Bish, D. L.; Johnston, C. T. Pressure-Controlled Polytypism in Hydrous Layered Materials. *Am. Mineral.* **2003**, *88*, 1428−1435.

(21) Hwang, H.; Seoung, D.; Lee, Y.; Liu, Z.; Liermann, H.-P.; Cynn, H.; Vogt, T.; Kao, C.-C.; Mao, H.-K. A Role for Subducted Super-Hydrated Kaolinite in Earth's Deep Water Cycle. *Nat. Geosci.* **2017**, *10*, 947−953.

(22) Hwang, H.; Choi, J.; Liu, Z.; Kim, D.-Y.; He, Y.; Celestian, A. J.; Vogt, T.; Lee, Y. Pressure-Induced Hydration and Formation of Bilayer Ice in Nacrite, a Kaolin-Group Clay. *ACS Earth Space Chem.* **2020**, *4*, 183−188.

(23) Plancon, A.; Giese, R. F.; Snyder, R.; Drits, V. A.; Bookin, A. S. Stacking Faults in the Kaolin-Group Minerals: Defect Structures of Kaolinite. *Clays Clay Miner.* **1989**, *37*, 203−210.

(24) Hinckley, D. N. Variability in "Crystallinity" Values among the Kaolin Deposits of the Coastal Plain of Georgia and South Carolina. In *Proceedings 11th National Conference, Ottowa, Ontario, in Ada Swineford*; Pergamon Press, New York: New York, 1963; pp. 229−235.

(25) Angel, R. J.; Bujak, M.; Zhao, J.; Gatta, G. D.; Jacobsen, S. D. Effective Hydrostatic Limits of Pressure Media for High-Pressure Crystallographic Studies. *J. Appl. Crystallogr.* **2007**, *40*, 26−32.

(26) Klotz, S.; Chervin, J.-C.; Munsch, P.; Le Marchand, G. Hydrostatic Limits of 11 Pressure Transmitting Media. *J. Phys. D: Appl. Phys.* **2009**, *42*, No. 075413.

(27) Mao, H. K.; Xu, J.; Bell, P. M. Calibration of the Ruby Pressure Gauge to 800 Kbar under Quasi-Hydrostatic Conditions. *J. Geophys. Res.* **1986**, *91*, 4673.

(28) Bassett, W. A.; Shen, A. H.; Bucknum, M.; Chou, I.-M. Hydrothermal Studies in a New Diamond Anvil Cell up to 10 GPa and from −190 C to 1200 C. *Pure Appl. Geophys.* **1993**, *141*, 487−495.

(29) Comodi, P.; Francesco Zanazzi, P. High-Pressure Structural Study of Muscovite. *Phys. Chem. Miner.* **1995**, *22*, 170−177.

(30) Brindley, G. W.; Robinson, K. Structure of Kaolinite. *Nature* **1945**, *156*, 661−662.

(31) Neder, R. B.; Burghammer, M.; Grasl, T. H.; Schulz, H.; Bram, A.; Fiedler, S. Refinement of the Kaolinite Structure from Single-Crystal Synchrotron Data. *Clays Clay Miner.* **1999**, *47*, 487−494.

(32) Farmer, V. C. Infrared Absorption of Hydroxyl Groups in Kaolinite. *Science* **1964**, *145*, 1189−1190.

(33) Ledoux, R. L.; White, J. L. Infrared Study of the OH Groups in Expanded Kaolinite. *Science* **1964**, *143*, 244−246.

(34) Ledoux, R. L.; White, J. L. Infrared Study of Selective Deuteration of Kaolinite and Halloysite at Room Temperature. *Science* **1964**, *145*, 47−49.

(35) Tosoni, S.; Doll, K.; Ugliengo, P. Hydrogen Bond in Layered Materials: Structural and Vibrational Properties of Kaolinite by a Periodic B3LYP Approach. *Chem. Mater.* **2006**, *18*, 2135−2143.

(36) Michaelian, K. H. The Raman Spectrum of Kaolinite #9 at 21°C. *Can. J. Chem.* **1986**, *64*, 285−294.

(37) Frost, R. L.; van der Gaast, S. J. Kaolinite Hydroxyls − a Raman Microscopy Study. *Clay Miner.* **1997**, *32*, 471−484.

(38) Frost, R. L.; Kloprogge, J. T. Raman Spectroscopy of the Low-Frequency Region of Kaolinite at 298 and 77 K. *Appl. Spectrosc.* **2016**, *53*, 1610−1616.

(39) Johnston, C. T.; Wang, S.-L.; Bish, D. L.; Dera, P.; Agnew, S. F.; Kenney, J. W., III Novel Pressure-Induced Phase Transformations in Hydrous Layered Materials. *Geophys. Res. Lett.* **2002**, *29*, 17-1−17-4.

(40) Newnham, R. E. A Refinement of the Dickite Structure and Some Remarks on Polymorphism in Kaolin Minerals. *Mineral. Mag. J. Mineral. Soc.* **1961**, *32*, 683−704.

(41) Mercier, P. H. J.; Le Page, Y. Kaolin Polytypes Revisited Ab Initio. *Acta Crystallogr. Sect. B Struct. Sci.* **2008**, *64*, 131−143.

(42) Mercier, P. H. J.; le Page, Y. Ab InitioExploration of Layer Slipping Transformations in Kaolinite up to 60 GPa. *Mater. Sci. Technol.* **2013**, *25*, 437−442.

(43) Basu, A.; Chandra, A.; Tyagi, A. K.; Mukherjee, G. D. Reappearance of Ferroelectric Soft Modes in the Paraelectric Phase of $Pb_{1-x}Ca_xTiO_3$ at High Pressures: Raman and x-Ray Diffraction Studies. *J. Phys. Condens. Matter* **2012**, *24*, 115404.

(44) Basu, A.; Jana, R.; Mandal, G.; Chandra, A.; Mukherjee, G. D. Pressure Driven Ferroelectric to Paraelectric Transition in Sr Doped BaTiO 3. *J. Appl. Phys.* **2015**, *117*, No. 054102.

(45) Bassett, W. A.; Shen, A. H.; Bucknum, M.; Chou, I.-M. A New Diamond Anvil Cell for Hydrothermal Studies to 2.5 GPa and from −190 to 1200 °C. *Rev. Sci. Instrum.* **1993**, *64*, 2340−2345.

(46) Bassett, W. A. High Pressure-Temperature Aqueous Systems in the Hydrothermal Diamond Anvil Cell (HDAC). *Eur. J. Mineral.* **2003**, *15*, 773−780.

(47) Pruzan, P.; Chervin, J. C.; Gauthier, M. Raman Spectroscopy Investigation of Ice VII and Deuterated Ice VII to 40 GPa. Disorder in Ice VII. *Europhys. Lett.* **1990**, *13*, 81−87.

(48) Walrafen, G. E.; Abebe, M.; Mauer, F. A.; Block, S.; Piermarini, G. J.; Munro, R. Raman and X-ray Investigations of Ice VII to 36.0 GPa. *J. Chem. Phys.* **1982**, *77*, 2166−2174.

(49) Carey, D. M.; Korenowski, G. M. Measurement of the Raman Spectrum of Liquid Water. *J. Chem. Phys.* **1998**, *108*, 2669−2675.

(50) Gatta, G. D.; Lee, Y. Zeolites at High Pressure: A Review. *Mineral. Mag.* **2014**, *78*, 267−291.

(51) Welch, M. D.; Kleppe, A. K.; Jephcoat, A. P. Novel High-Pressure Behavior in Chlorite: A Synchrotron XRD Study of Clinochlore to 27 GPa. *Am. Mineral.* **2004**, *89*, 1337−1340.

(52) Welch, M. D. A High-Pressure Polytypic Transformation in Type-I Chlorite. *Am. Mineral.* **2005**, *90*, 1139−1145.

(53) Mookherjee, M.; Stixrude, L. Structure and Elasticity of Serpentine at High-Pressure. *Earth Planet. Sci. Lett.* **2009**, *279*, 11−19.

(54) Chheda, T. D.; Mookherjee, M.; Mainprice, D.; dos Santos, A. M.; Molaison, J. J.; Chantel, J.; Manthilake, G.; Bassett, W. A. Structure and Elasticity of Phlogopite under Compression: Geophysical Implications. *Phys. Earth Planet. Inter.* **2014**, *233*, 1−12.

(55) McKinstry, H. A. Thermal Expansion of Clay Minerals. *Am. Mineral.* **1965**, *50*, 212−222.

(56) Mookherjee, M.; Redfern, S. A. T.; Zhang, M. Thermal Response of Structure and Hydroxyl Ion of Phengite 2M1: An in Situ Neutron Diffraction and FTIR Study. *Eur. J. Mineral.* **2001**, *13*, 545−555.

(57) Zanazzi, P. F.; Pavese, A. Behavior of Micas at High-Pressure and High-Temperature. *Rev. Mineral. Geochem.* **2002**, *46*, 99−116.

(58) Chinnery, N. J.; Pawley, A. R.; Clark, S. M. In Situ Observation of the Formation of 10 Å Phase from Talc + H_2O at Mantle Pressures and Temperatures. *Science* **1999**, *286*, 940−942.

(59) Rashchenko, S. V.; Kamada, S.; Hirao, N.; Litasov, K. D.; Ohtani, E. In Situ X-Ray Observation of 10 Å Phase Stability at High Pressure. *Am. Mineral.* **2016**, *101*, 2564−2569.

(60) You, S.; Kunz, D.; Stöter, M.; Kalo, H.; Putz, B.; Breu, J.; Talyzin, A. V. Pressure-Induced Water Insertion in Synthetic Clays. *Angew. Chem. Int. Ed.* **2013**, *52*, 3891−3895.

(61) Gleason, A. E.; Parry, S. A.; Pawley, A. R.; Jeanloz, R.; Clark, S. M. Pressure-Temperature Studies of Talc plus Water Using X-Ray Diffraction. *Am. Mineral.* **2008**, *93*, 1043−1050.

(62) Johnston, C. T. Probing the Nanoscale Architecture of Clay Minerals. *Clay Miner.* **2010**, *45*, 245−279.

(63) Sano, A.; Ohtani, E.; Kondo, T.; Hirao, N.; Sakai, T.; Sata, N.; Ohishi, Y.; Kikegawa, T. Aluminous Hydrous Mineral δ -AlOOH as a Carrier of Hydrogen into the Core-Mantle Boundary. *Geophys. Res. Lett.* **2008**, *35*, L03303.

(64) Guggenheim, S.; Koster van Groos, A. F. New Gas-Hydrate Phase: Synthesis and Stability of Clay−Methane Hydrate Intercalate. *Geology* **2003**, *31*, 653.

(65) Bentabol, M.; Cruz, M. D. R. Characterization of Tobelite Formed from Kaolinite under Hydrothermal Conditions (200°C). *Appl. Clay Sci.* **2016**, *126*, 160−172.

(66) Mookherjee, M.; Redfern, S. A. T.; Zhang, M.; Harlov, D. E. Orientational Order-Disorder of N(D,H) 4^+ in Tobelite. *Am. Mineral.* **2002**, *87*, 1686−1691.

(67) Mookherjee, M.; Redfern, S. A. T. A High-Temperature Fourier Transform Infrared Study of the Interlayer and Si−O-Stretching Region in Phengite-2M_1. *Clay Miner.* **2002**, *37*, 323−336.

(68) Watenphul, A.; Wunder, B.; Heinrich, W. High-Pressure Ammonium-Bearing Silicates: Implications for Nitrogen and Hydrogen Storage in the Earth's Mantle. *Am. Mineral.* **2009**, *94*, 283−292.

(69) Wunder, B.; Rubie, D. C.; Ross, C. R.; Medenbach, O.; Seifert, F.; Schreyer, W. Synthesis, Stability, and Properties of $Al_2SiO_4(OH)_2$: A Fully Hydrated Analogue of Topaz. *Am. Mineral.* **1993**, *78*, 285−297.

(70) Peng, Y.; Mookherjee, M.; Hermann, A.; Bajgain, S.; Liu, S.; Wunder, B. Elasticity of Phase-Pi ($Al_3Si_2O_7(OH)_3$) − A Hydrous Aluminosilicate Phase. *Phys. Earth Planet. Inter.* **2017**, *269*, 91−97.

(71) Frost, R. L. Fourier Transform Raman Spectroscopy of Kaolinite, Dickite and Halloysite. *Clays Clay Miner.* **1995**, *43*, 191−195.

(72) Lee, Y.; Kim, P.; Kim, H.; Seoung, D. Comparative Compressibility of Smectite Group under Anhydrous and Hydrous Environments. *Materials (Basel).* **2020**, *13*, 3784.